Ca_3AlSb_3: an inexpensive, non-toxic thermoelectric material for waste heat recovery

Alex Zevalkink,[a] Eric S. Toberer,[a] Wolfgang G. Zeier,[a] Espen Flage-Larsen[b] and G. Jeffrey Snyder*[a]

Received 1st October 2010, Accepted 9th November 2010
DOI: 10.1039/c0ee00517g

Thermoelectric materials directly convert thermal energy into electrical energy, offering a promising solid-state solution for waste heat recovery. For thermoelectric devices to make a significant impact on energy and the environment the major impediments are the efficiency, availability and toxicity of current thermoelectric materials. Typically, efficient thermoelectric materials contain heavy elements such as lead and tellurium that are toxic and not earth abundant. Many materials with unusual structures containing abundant and benign elements are known, but remain unexplored for thermoelectric applications. In this paper we demonstrate, with the discovery of high thermoelectric efficiency in Ca_3AlSb_3, the use of elementary solid-state chemistry and physics to guide the search and optimization of such materials.

Introduction

Thermoelectric devices, which directly convert thermal energy to electrical energy, have the potential to play a significant role in averting a global energy crisis. While thermoelectrics are currently found in extraterrestrial and other specialized applications, this solid state technology could be readily harnessed to convert the vast quantities of automobile and industrial waste heat into useful energy. Despite the longevity and scalability of current devices, further improvements in cost and efficiency are required for thermoelectric generators to be competitive.

The thermoelectric efficiency of a material is governed by its thermoelectric figure of merit, or zT ($zT = \alpha^2T/\rho\kappa$). Therefore, a material suitable for thermoelectric applications must have a large Seebeck coefficient (α), low resistivity (ρ) and low thermal conductivity (κ). This combination of properties is difficult to obtain due to the strongly coupled nature of α, ρ, and the electronic component of κ.[1] The lattice component of the thermal conductivity is generally considered to be the most decoupled property in zT, and is therefore often the focus of thermoelectric research. A trend between low lattice thermal conductivity and structural complexity has led to a particular interest in materials with complex crystal structures.[2–4]

In addition to material efficiency, the widespread use of thermoelectric energy generation is also limited by the expense and toxicity of current thermoelectric materials (*e.g.* PbTe).[5] Zintl compounds based on antimony and alkali and alkaline earth metals are a potential source of environmentally benign, Earth-abundant, and inexpensive materials.[2,6,7] Zintl compounds are composed of electropostive cations that donate electrons to the more electronegative anions, which must in turn form covalent bonds to satisfy valence.[8,9] The resulting mix of ionic and covalent bonding frequently leads to complex crystal structures with large unit cells. Good thermoelectric performance is generally found in heavily-doped semiconductors with carrier concentrations on the order of 10^{19} to 10^{21} carriers/cm^3.[1] It is therefore important to be able to control carrier concentration in Zintl compounds *via* doping. This has been successfully demonstrated in several Zintl antimonides including $Ca_5Al_2Sb_6$, and $Yb_{14}AlSb_{11}$.[10–13]

Within the A_3AlSb_3 compounds (A = alkaline earth metals), two structure types are known; Ca_3InP_3 (*Pnma*) and Ba_3AlSb_3 (*Cmca*). Ca_3AlSb_3 forms in the Ca_3InP_3 structure type, composed of infinite chains of corner-sharing $AlSb_4$ tetrahedra (Fig. 1).[14] In contrast, the Ba_3AlSb_3 structure type contains isolated pairs of edge-sharing $AlSb_4$ tetrahedra, yielding $A1_2Sb_6$

[a]*Materials Science, California Institute of Technology, 1200 E. California Blvd., Pasadena, California, 91125, USA. E-mail: jsnyder@caltech.edu*
[b]*Department of Physics, University of Oslo, P.O. Box 1048, Blindern, N-0316, Norway*

Broader context

Thermoelectric materials directly convert thermal energy into electrical energy. The widespread implementation of thermoelectric generators is limited by both the low efficiency and by the cost and toxicity of state-of-the-art materials. In order to address these limitations, much effort has been focused on exploring compounds that are composed of non-toxic and Earth-abundant elements. Here we report the electronic and thermal transport properties of a promising and inexpensive new thermoelectric material, Ca_3AlSb_3. Through substitution of sodium on the calcium site, control and optimization of the hole carrier concentration is obtained. Ca_3AlSb_3 is found to have an exceptionally low lattice thermal conductivity (0.6 W/mK at 1050 K), due in large part to its complex unit cell. The combination of a reasonable bandgap, good carrier concentration control and low thermal conductivity yields a thermoelectric figure of merit (zT) of 0.8. Further improvements in the thermoelectric efficiency of Ca_3AlSb_3 can be expected through band structure engineering and the inclusion of point and extended defects to scatter phonons.

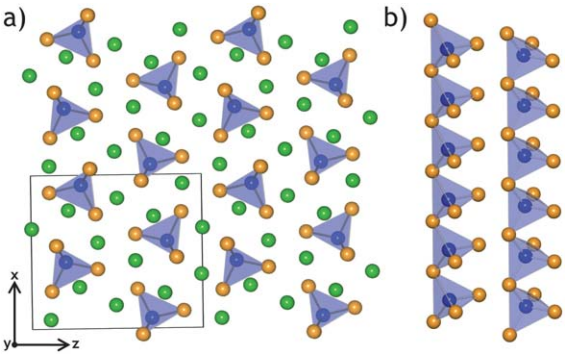

Fig. 1 (a) Orthorhombic unit cell of Ca_3AlSb_3 (space group *Pnma*) viewed in the [010] direction. (b) Infinite chains of corner sharing $AlSb_4$ tetrahedra. Sb atoms are orange, Ca are green, and Al are blue.

anionic units.[15,16] In both structure types, the *A* ions are situated between the tetrahedra moieties and provide overall charge balance.

Within the Zintl formalism, Ca_3AlSb_3 can be expressed as $Ca_3^{+2}Al_1^{-1}Sb_2^{-2}Sb_1^{-1}$, treating Al as part of the covalent anionic substructure. The aluminium atoms are bound to four antimony atoms, and therefore have a valence of −1. Within the chains of $AlSb_4$ tetrahedra, the antimony atoms that are shared between two tetrahedra have two bonds and can be considered to have a valence of −1. The remaining antimony have only one bond, corresponding to a valence of −2. Situated between the chains are Ca^{+2} ions, which provide overall charge balance. The formal valences given here are a convenient construct, however, the actual extent of charge transfer is determined by electronegativity and the degree of ionic or covalent bonding. Treating Al as a cation yields the same conclusion; namely, Ca_3AlSb_3 is charge balanced.

Inspired by our previous investigation of the thermoelectric properties of sodium-doped $Ca_5Al_2Sb_6$,[13] this work focuses on the high temperature thermal and electronic properties of $Ca_{3-x}Na_xAlSb_3$ ($x = 0$, 0.03, 0.06, and 0.15). In addition to transport measurements, this study employs a combination of classic transport theory and electronic structure calculations to improve our understanding of the relationship between chemical bonding and transport in Ca_3AlSb_3. The structure of Ca_3AlSb_3 is similar to $Ca_5Al_2Sb_6$ in that both are composed of infinite parallel chains of $AlSb_4$ tetrahedra. Compared with Ca_3AlSb_3, the relative deficiency of Ca in $Ca_5Al_2Sb_6$ leads to fewer electrons, therefore requiring covalent Sb–Sb bonds to fulfill valance balance. These additional bonds link the parallel chain moieties together, resulting in ladder-like structures, in contrast to the isolated chains of Ca_3AlSb_3. Beyond Ca_3AlSb_3 and $Ca_5Al_2Sb_6$, a variety of structure types with distinct tetrahedra moieties exist within the A_3MPn_3 and $A_5M_2Pn_6$ compounds, offering further opportunities for developing structure-property relationships in Zintl compounds.[8,9,17]

Experimental

Synthesis

Bulk, polycrystalline $Ca_{3-x}Na_xAlSb_3$ ($x = 0$, 0.03, 0.06, 0.15) samples were prepared by ball milling followed by hot pressing. Starting with 99.99% pure Ca dendrites from Sigma-Aldrich, and from Alpha Aesar: 99.95% Na chunks, 99% Al shot, and 99.5% Sb lumps, the elements were loaded into stainless-steel vials with stainless-steel balls in an argon-filled glove box. The reagents were milled for 90 min using a SPEX Sample Prep 8000 Series Mixer/Mill. The resulting fine powder was hot pressed in high density graphite dies (POCO) using 1.2 tons of force on a 12 mm diameter surface. A maximum temperature of 973 K for two hours in argon was used during hot pressing, followed by a stress-free anneal at 873 K and a three hour cool down under vacuum. Care was taken in every step to avoid oxidation of the powder.

Characterization

The polycrystalline ingots resulting from hot pressing were sliced into disks 1 mm thick and 12 mm in diameter. X-Ray diffraction (XRD) measurements were performed on polished slices using a Philips XPERT MPD diffractometer operated at 45 kV and 40 mA, and Rietveld analysis was performed using Philips X'Pert Plus software. XRD analysis and scanning electron microscopy using a Zeiss 1550 VP SEM was used to determine phase purity. Microprobe analysis with wavelength dispersive spectroscopy (WDS) using a JEOL JXA-8200 system was used to determine sodium content. Elemental Al and Sb, $NaAlSi_3O_8$, and $CaA1_2Si_2O_8$ were used for the Al, Sb, Na, and Ca standards, respectively. The high temperature electronic properties were characterized to 1073 K under dynamic vacuum at the Jet Propulsion Laboratory; electrical resistivity was determined using the Van der Pauw technique, and the Hall coefficient was measured with a 1.0 T field and pressure-assisted contacts. Details of the Seebeck coefficient measurements can be found in ref. 19. A Netzsch LFA 457 was used to measure thermal diffusivity to 1073 K and the heat capacity was estimated using the method of Dulong-Petit.

Electronic structure calculations

Electronic structure calculations were performed in the Vienna *Ab -initio* Simulation Package (VASP).[20,21] For the exchange and correlation the Perdew-Burke-Enzerhof generalized gradient approximation (PBE-GGA)[22] functional was used in the projector augmented-wave (PAW) formalism.[23] The experimental lattice constants and atom positions reported by Cordier *et al.* were used as input.[14] A *k*-point grid of $5 \times 15 \times 5$ and an energy cutoff of 450 eV were necessary to converge the total energy to within a few meV.

In addition to the density of states and band structure, we present real-space analysis of the bonds in the structure. The electron density difference (EDD) employed here is the difference between the electron density of the crystal and the overlapping, non-bonding, atomic electron densities (procrystal).[24] The procrystal electron density is obtained by super-position of the electron density of the respective atoms in vacuum. For both the crystal and the procrystal, all-electron densities was regenerated after the initial run.

Results and discussion

Ball milling of elemental reagents followed by hot pressing resulted in samples with densities in excess of 95%. X-Ray

diffraction (XRD) patterns of each polycrystalline sample ($x = 0$, 0.03, 0.06, 0.15) are shown in Fig. 2. As the ionic radii of Na^{+1} and Ca^{+2} are nearly identical, no change in lattice parameter is expected from doping. XRD patterns were subject to Rietveld refinement using the known structures of Ca_3AlSb_3 and $Ca_5Al_2Sb_6$. Fig. 2a shows the Ca_3AlSb_3 and $Ca_5Al_2Sb_6$ components of the Rietveld fit for the $x = 0$ sample, as well as a difference profile.

All compositions were found to contain approximately 10 wt.% of the closely related $Ca_5Al_2Sb_6$ phase, possibly due to inadvertent Ca deficiency. Cordier *et al.* have also reported $Ca_5Al_2Sb_6$ as a secondary phase in their efforts to synthesize pure Ca_3AlSb_3.[14]

SEM images of polished and fracture surfaces of the $x = 0.06$ sample are shown in Fig. 3. Scanning electron microscopy confirms the high density of the samples and reveals grains with diameters of approximately 1 μm. The small grain size may be due to the presence of $Ca_5Al_2Sb_6$ impurity phase pinning grain boundaries during growth or the relatively low hot-pressing temperature (973 K).

Microprobe analysis with wavelength dispersive spectroscopy (WDS) was used to verify stoichiometry and to quantify the incorporation of sodium in Ca_3AlSb_3. Microprobe analysis also confirmed the presence of the $Ca_5Al_2Sb_6$ impurity phase in all samples. This phase appears as approximately 1 μm grains, evenly distributed within the Ca_3AlSb_3 majority phase. In the $x = 0.15$ sample, a sodium-rich impurity phase was also identified, suggesting that this sample exceeded the solubility limit of sodium in Ca_3AlSb_3. Fig. 4 shows the sodium concentration obtained from WDS *versus* the synthetic sodium content. The unfilled symbols represent the average sodium concentration of each sample (includes the sodium-rich phase in $x = 0.15$ sample), obtained using a spot size of 30 μm averaged over

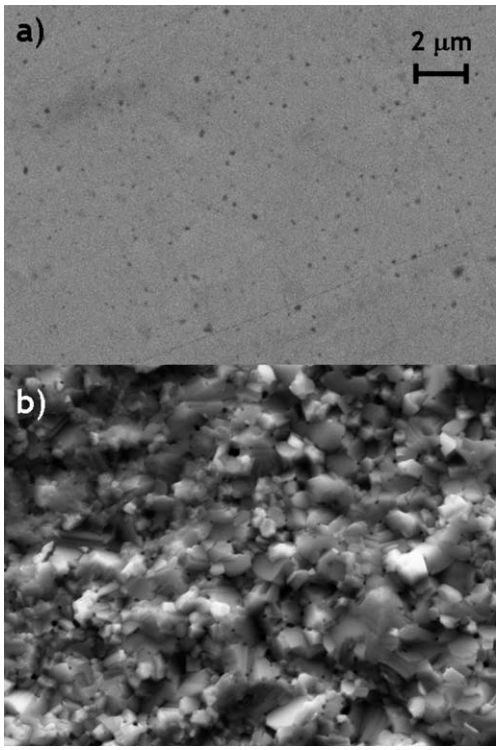

Fig. 3 Scanning electron micrographs of (a) polished and (b) fractured surfaces of the $x = 0.06$ sample reveal high density material and approximately 1 μm diameter grains. Black dots in (a) are voids revealed by polishing.

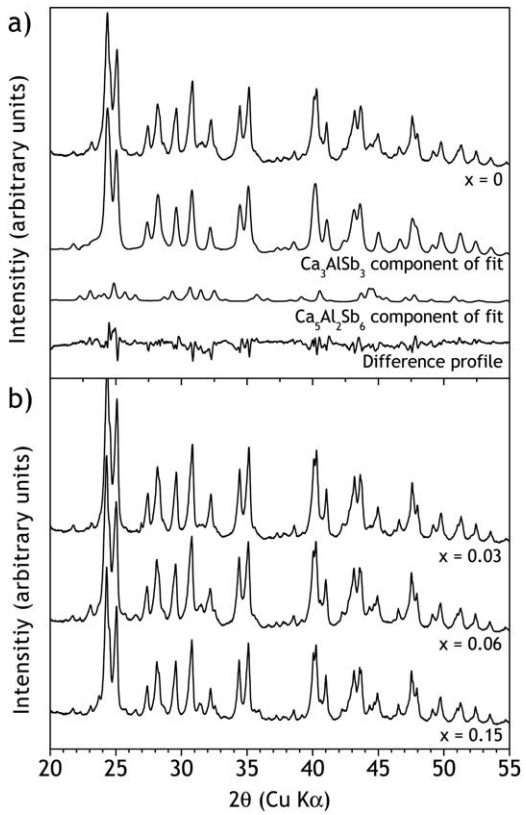

Fig. 2 (a) XRD pattern of $x = 0$ sample and Rietveld fit using known crystal structures of Ca_3AlSb_3 and $Ca_5Al_2Sb_6$.[14,18] (b) Similar amounts of $Ca_5Al_2Sb_6$ impurity phase are observed in all sodium doped samples.

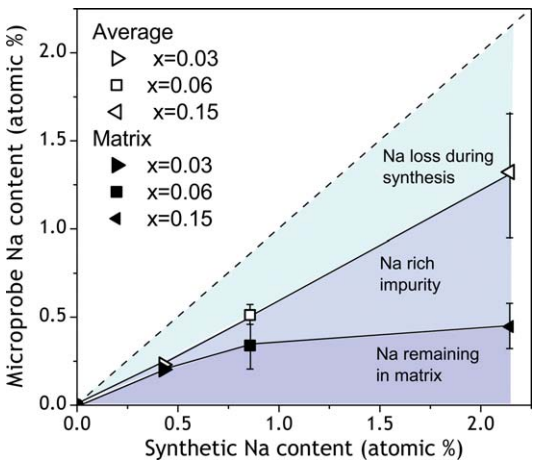

Fig. 4 Microprobe analysis suggests that some sodium loss occurs during synthesis, and that the solubility limit of sodium in $Ca_{3-x}Na_xAlSb_3$ is exceeded for $x > 0.06$ (0.8 atomic %). Filled symbols indicate Na content of the matrix phases (Ca_3AlSb_3 and $Ca_5Al_2Sb_6$), while unfilled symbols represent total Na concentration, including the sodium rich impurity phase.

25 points on each sample. The deviation of the average sample sodium content from expected composition is attributed to sodium loss during synthesis. The filled symbols show the sodium content of the matrix, which consists of the Ca_3AlSb_3 and $Ca_5Al_2Sb_6$ phases. The large discrepancy between the average and matrix sodium concentration for the $x = 0.15$ sample is due to the formation of the sodium rich impurity phase which makes an estimated 5 to 10 volume % of the sample.

Electronic transport properties

The electronic and thermal properties of sodium doped $Ca_5Al_2Sb_6$ have been previously investigated,[13] and are similar to those reported here for sodium doped Ca_3AlSb_3. In light of this, and as the volume fraction of the Ca_3AlSb_3 phase is far greater than that of the $Ca_5Al_2Sb_6$ minority, the properties reported here should be close to those expected from phase pure Ca_3AlSb_3.

From the Zintl valence-counting formalism, nominally undoped Ca_3AlSb_3 is expected to be an intrinsic semiconductor. In practice, extrinsic defects lead to a measured Hall carrier concentration ($n_H = 1/R_He$) of 10^{18} h^+/cm^3 at room temperature. The room temperature n_H *versus* microprobe sodium content is shown in Fig. 5. The carrier concentration expected from simple charge counting, assuming that each sodium atom contributes one free hole, is shown as a dashed line. Comparing the measured carrier concentrations to those predicted from charge counting, one finds that the experimental n_H is significantly less than predicted. This is analogous to the low doping effectiveness observed in sodium doped $Ca_5Al_2Sb_6$.[13]

Fig. 6 illustrates the temperature dependence of n_H. Nominally undoped Ca_3AlSb_3 exhibits increasing carrier concentration due to carrier activation beginning at 500 K. For the sodium doped samples, n_H remains constant with temperature to approximately 800 K, indicative of extrinsic doping. The abrupt increase in carrier concentration beyond 800 K may be due to activation of minority carriers across the band gap, an increase in majority carrier concentration due to dopant solubility variation, or a phase change.

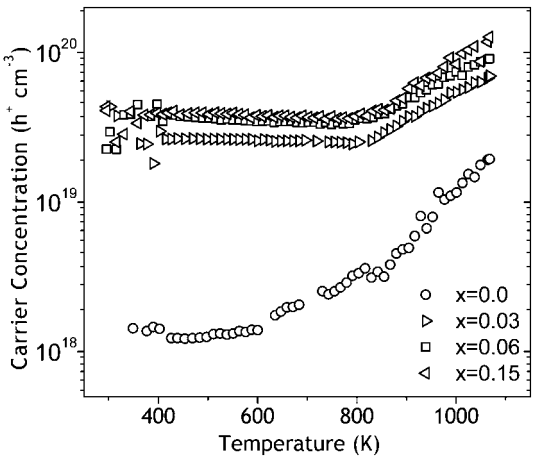

Fig. 6 Hall carrier concentration of $Ca_{3-x}Na_xAlSb_3$ as a function of temperature. Doped samples exhibit extrinsic behavior to 800 K.

The Hall mobility as a function of temperature, calculated from measured R_H and resistivity (ρ), is shown in Fig. 7. Matthiessen's rule approximates electronic mobility as the reciprocal sum of multiple mobility terms, each having an independent scattering mechanism $\left(\frac{1}{\mu} = \sum_i \frac{1}{\mu_i}\right)$. Generally, one scattering mechanism limits the total mobility at extreme temperature ranges. In Ca_3AlSb_3, the mobility increases with temperature up to 600 K, possibly due to activation barriers such as oxide layers at the grain boundaries. Such an activated mobility would exhibit an exponential temperature dependence ($\mu = \mu_o e^{-E_A/k_bT}$). At high temperatures, mobility is generally limited by acoustic phonon scattering, for which the temperature dependence is given by the power law, $\mu_H \propto T^{-\nu}$, where ν is 1.5 for nondegenerate semiconductors and 1 for degenerate semiconductors.[25] A power law fit to the high temperature mobility data shown in Fig. 7 results in an exponent larger than 1.5. This may be related to the abrupt increase in carrier concentration above 800 K observed in Fig. 6, or a temperature dependent effective mass.

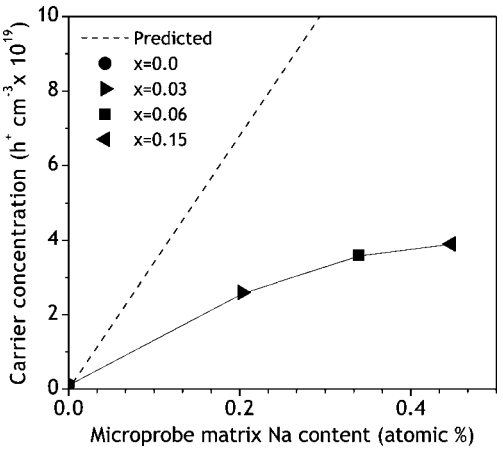

Fig. 5 Hall carrier concentration (300 K) increases as a function of sodium content, although doping effectiveness is less than predicted by charge counting.

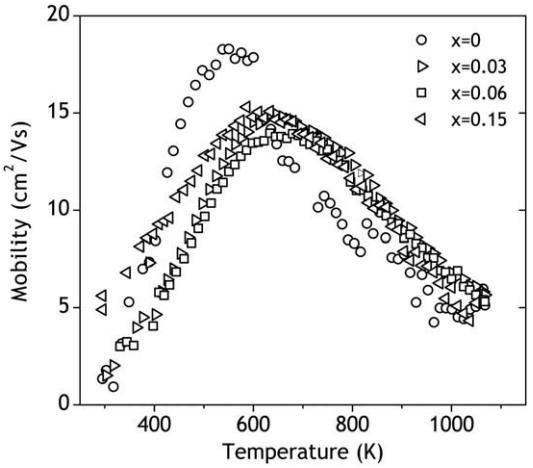

Fig. 7 Temperature dependence of Hall mobility in $Ca_{3-x}Na_xAlSb_3$ suggests an activated mobility at low temperature, and a mobility limited by phonon scattering at high temperature.

The temperature dependence of the resistivity (Fig. 8) follows from the carrier concentration and mobility ($\rho = 1/ne\mu$). At high temperature, the resistivity of the nominally undoped sample exhibits an exponential decrease due to carrier activation across a band gap (Fig. 8, inset). A band gap of ~0.6 eV was estimated from the slope of the resistivity in this presumably intrinsic high temperature regime ($\rho \propto e^{E_g/2kT}$). This is similar to the band gap observed in both $Yb_{14}AlSb_{11}$ (0.5 eV) and in $Ca_5Al_2Sb_6$ (0.5 eV). Doping Ca_3AlSb_3 with sodium results in reduced resistivity due to increased carrier concentration. For the undoped and doped compositions, the negative slope of the resistivity at low temperatures is due to the increasing mobility in that temperature range. From 600–800 K, the resistivities of the sodium doped samples begin to increase with temperature as is expected for a degenerate semiconductor with mobility limited by phonon scattering. However, above 800 K, this trend is reversed, and the resistivity begins to decrease again due to the carrier activation discussed above.

Fig. 9 illustrates the effect of doping on the Seebeck coefficients measured at 700 K. The Seebeck coefficients are large and positive, consistent with the relatively low carrier concentrations revealed by Hall effect measurements. As expected, increasing carrier concentration leads to a decrease in Seebeck coefficient. Solutions to the Boltzmann transport equation within the relaxation time approximation have been used to model the relationship between carrier concentration and the Seebeck coefficient *via* the reduced chemical potential, η (eqn (1) and 2).[26,27] The full expression for the Fermi integral, $F_j(\eta)$ is given in eqn (3), where ζ is the reduced carrier energy. Here, we assume a single carrier type is dominant, allowing use of a single parabolic band (SPB) model, and we assume $\lambda = 0$ (acoustic phonon scattering).

$$\alpha = \frac{k}{e}\left(\frac{(2+\lambda)F_{1+\lambda}(\eta)}{(1+\lambda)F_{\lambda}(\eta)} - \eta\right) \quad (1)$$

$$n = 4\pi\left(\frac{2m^* k_b T}{h^2}\right)^{3/2} F_{1/2}(\eta) \quad (2)$$

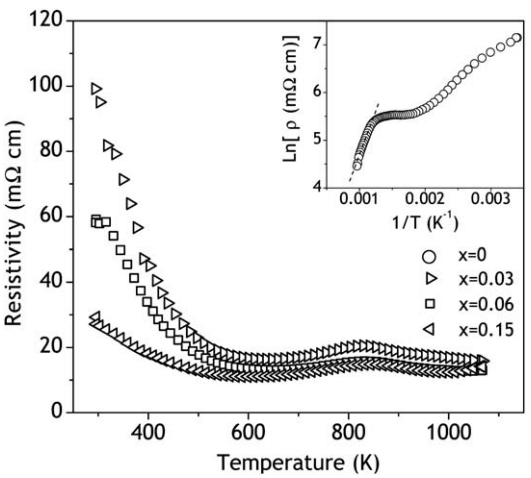

Fig. 8 Resistivity of $Ca_{3-x}Na_xAlSb_3$ as a function of temperature for heavily doped samples $x = 0.03, 0.06, 0.15$. Inset: Ln[ρ] *versus* 1/T for $x = 0$ sample. The high temperature linear fit results in a band gap of 0.6 eV using $\rho \propto e^{E_g/2k_bT}$.

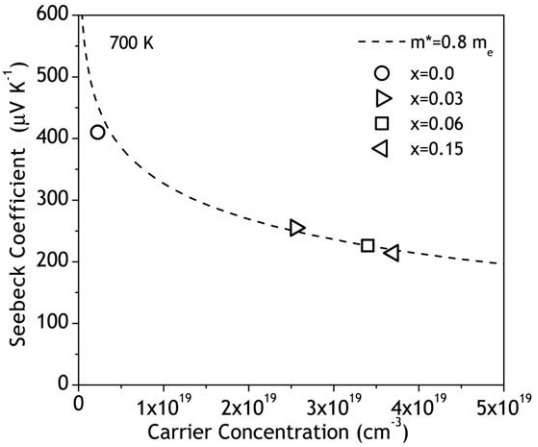

Fig. 9 Experimental Seebeck coefficients of $Ca_{3-x}Na_xAlSb_3$ as a function of carrier concentration. The dotted line was generated using a single parabolic band approximation and an effective mass of 0.8 m_e.

$$F_j(\eta) = \int_0^{\infty} \frac{\zeta^j d\zeta}{1 + Exp(\zeta - \eta)} \quad (3)$$

We employ this model at 700 K because in this temperature regime acoustic phonon scattering becomes the dominant scattering mechanism, and extrinsic carriers still dominate electronic transport. An effective mass of 0.8 m_e was calculated for this temperature using the measured α and n_H from the $x = 0.06$ sample in eqn (1)–(3). This effective mass was used to generate a Pisarenko curve at 700 K, shown as the dashed line in Fig. 9. All of the samples fall on or near this curve, suggesting that the effective mass remains fairly constant within this carrier concentration range.

The trends in Seebeck coefficient as a function of temperature are shown in Fig. 10. The Seebeck coefficient of the nominally undoped sample peaks at 650 K, at which point thermally activated electrons cause a reduction in thermoelectric voltage, and a decaying Seebeck coefficient results. Samples with $x = 0.03$–0.15 exhibit increasing Seebeck coefficients to high temperature,

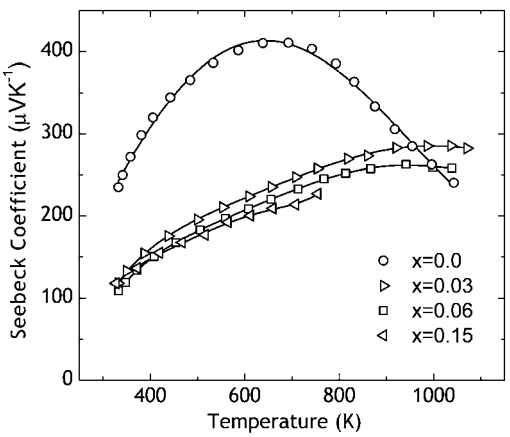

Fig. 10 High temperature Seebeck coefficients of $Ca_{3-x}Na_xAlSb_3$ show degenerate behavior for the extrinsically doped, p-type compositions.

as expected for extrinsic semiconductors. At 1000 K, the $x = 0.06$ sample appears to peak at 260 μV/K. From this, a band gap of 0.5 eV is estimated using $E_g = 2e\alpha_{max}T_{max}$.[28]

Electronic structure calculations

Density functional theory calculations (DFT) are used here to gain a better understanding of electronic behavior in this compound and to guide chemical strategies for further optimization. The band structure of Ca_3AlSb_3 is shown in the top panel of Fig. 11, while the bottom panel displays only the top of the valence band. Centered at the Γ point, the valence band edge contains two asymmetric, overlapping bands which give the appearance of nested, parabolic light and heavy bands, as well as an offset band with a maximum at −0.13 eV. Parabolic fits are used to estimate the band masses of the effective light and heavy bands, as well as the offset band. The blue, yellow and green solid curves in the bottom panel of Fig. 11 are parabolas with effective masses of 0.15, 0.75, and 0.9 m_e respectively. The most heavily doped sample in this study has a carrier concentration of 4×10^{19} h^+/cm^3, corresponding to a Fermi level of approximately ~0.1 eV below the valence band edge. This suggests that the doped samples in this study have energies spanning the three highlighted bands at the top of the valence band. The electronic transport data reported here is reasonably well described by a single parabolic band model (Fig. 9). However, from Fig. 11, one might expect to observe a carrier concentration dependent effective mass. In particular, by doping to higher carrier concentrations (>5×10^{19} h^+/cm^3) to probe deeper into the valence band, a larger effective mass and non-SPB behavior may result, due to the ever-increasing influence of the offset band (highlighted by the green curve in Fig. 11). This would be similar to the off-set band behavior observed in La_3Te_4.[29]

The Ca_3InP_3 structure type accomodates a considerable number of substitutions: Ca can be replaced by Sr, Ba, and Eu; In by Al and Ga; and P by As and Sb. Considering both isoelectronic substitutions and potential dopants, there are numerous routes to influencing the transport properties of this compound. To understand the potential effects of these substitutions, investigation of the bonding character in Ca_3AlSb_3 is essential.

The traditional quantum mechanical description of covalent bonding is characterized by charge build-up between atoms. Thus, an intuitive approach to locating covalent bonds is to determine the location of increased electron density. This approach is pursued here, through post-processing of DFT calculations, which aids in the visualization of electron density reorganization. Electron density difference (EDD) maps have been generated by subtracting the super-positioned, non-interacting, atomic electron densities (procrystal) from the calculated electron density of Ca_3AlSb_3.[24] EDD line-scans, shown in Fig. 12, illustrate the charge accumulation and depletion along both Al–Sb and Ca–Sb bonds. Part (a) shows an Al–Sb bond forming the backbone of a tetrahedra chain (green curve) and two distinct Al–Sb bonds perpendicular to the chain (blue and orange curves). Symmetric accumulation of electron density between the atoms indicates that the Al–Sb bonds have covalent character, consistent with our understanding of bonding within the Zintl construct. This electron accumulation shows surprising symmetry, considering the large disparity in electronegativity of Al and Sb. In contrast, representative Ca–Sb line scans, shown in Fig. 12b, exhibit significant asymmetry in charge distribution, with the principle charge build-up nearer to the Sb side. EDD line scans of $SrZn_2Sb_2$ have shown similar features.[30] To further illustrate the bonding environment in Ca_3AlSb_3, EDD isosurfaces in Fig. 13 depict (a) charge accumulation and (b) depletion. Charge build-up at the mid-point between the Al and Sb atoms, indicative of covalent bonding, is readily observed.

As discussed above in reference to Fig. 11, the effective mass at the band edge is fundamental to electron transport. To engineer

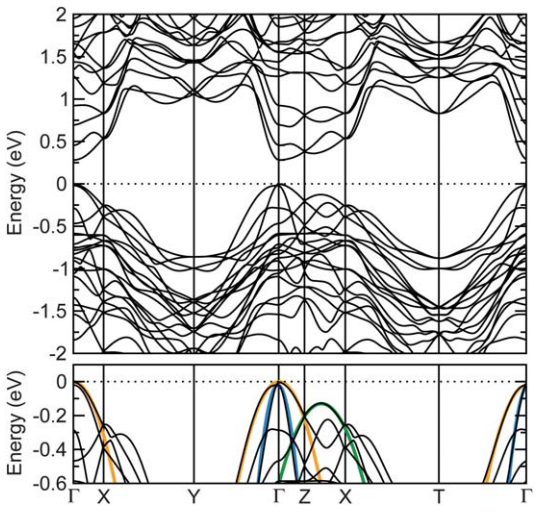

Fig. 11 Top panel: Calculated band structure of Ca_3AlSb_3. Bottom panel: Magnified band structure at the top of the valence band. The highest carrier concentration obtained experimentally corresponds to ~0.1 eV below the valence band edge. The blue, yellow, and green dashed curves are parabolas with effective masses of 0.15, 0.75, and 0.9 m_e.

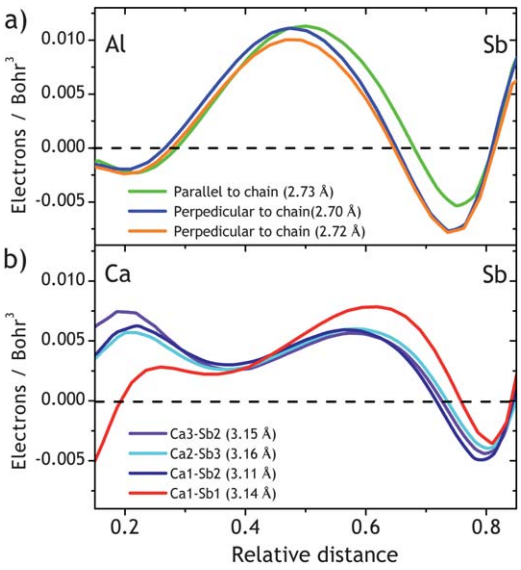

Fig. 12 (a) EDD line-scans show charge accumulation and depletion along a chain-forming Al–Sb bond (green), and two distinct Al–Sb bonds perpendicular to the chains (blue and orange). (b) Representative Ca–Sb bonds (site designations correspond to ref. 14).

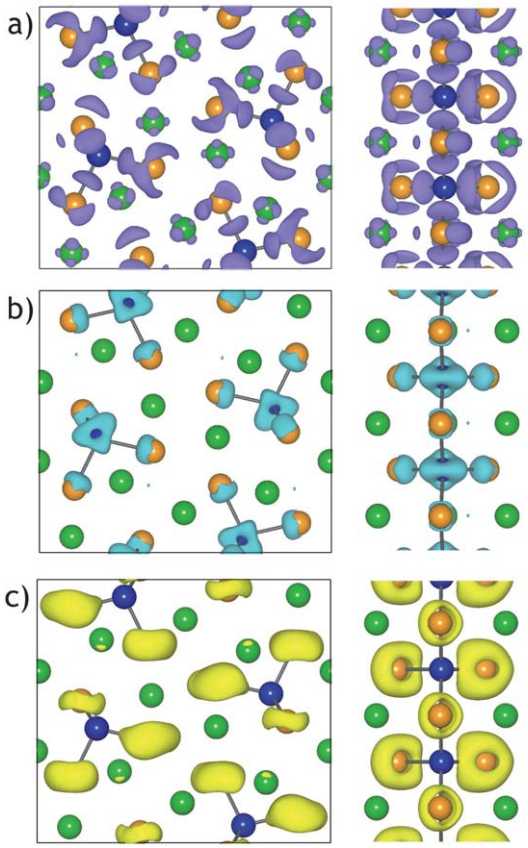

Fig. 13 EDD isosurfaces show (a) accumulation (b) and depletion regions. (c) Electron density map of valence band edge (−0.1 eV). Images are projections along [010] (left side) and [201] (right side) directions.

transport properties in this material, it is therefore important to have some understanding of the character of the valence band edge. Density of states calculations (DOS) (Fig. 14) indicate that Sb *p* states are a major component of the valence band edge,

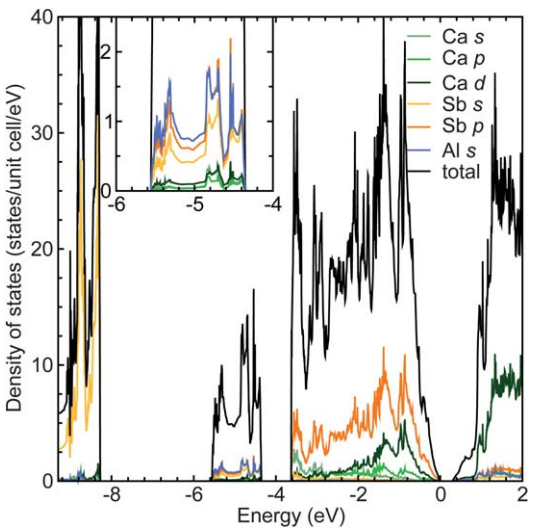

Fig. 14 Density of states of Ca_3AlSb_3 reveals a band gap at the Fermi level with a valence band edge dominated by Sb *p* states. The inset highlights interacting Al–Sb states.

analogous to the calculated density of states for the AZn_2Sb_2 Zintl antimonides.[30] The isosurfaces in Fig. 13c illustrate the electron charge density at a specific energy near the valence band edge (−0.1 eV). The electron charge density is highest around the Sb sites, where oriented donut-like isosurfaces form, suggesting hole transport, and therefore hole mobility, is centered around the tetrahedral Sb, as has been found in the structurally related $A_{14}MPn_{11}$.[31] It is interesting to note that the light bands shown in the DOS span the Γ–Y, Γ–Z, and Γ–T directions, corresponding to the y–z plane containing the donut-like charge density isosurfaces.

Thermal transport properties

Thermal diffusivity was measured to 1073 K. The thermal conductivity was calculated using $\kappa = D\rho C_p$ where D =thermal diffusivity, ρ = geometric density, C_p = heat capacity. Here, use of the Dulong–Petit approximation for the heat capacity (C_p = 0.34 J/g K) is likely to result in an underestimation of the thermal conductivity at high temperatures. In addition, there is 3% uncertainty inherent in laser flash diffusivity measurements. Total thermal conductivity, shown in Fig. 15a, is a combination of lattice, electronic, and bipolar contributions ($\kappa_{total} = \kappa_L + \kappa_e + \kappa_B$). The Wiedemann–Franz relation $\left(\kappa_e = \frac{LT}{\rho}\right)$ is used to

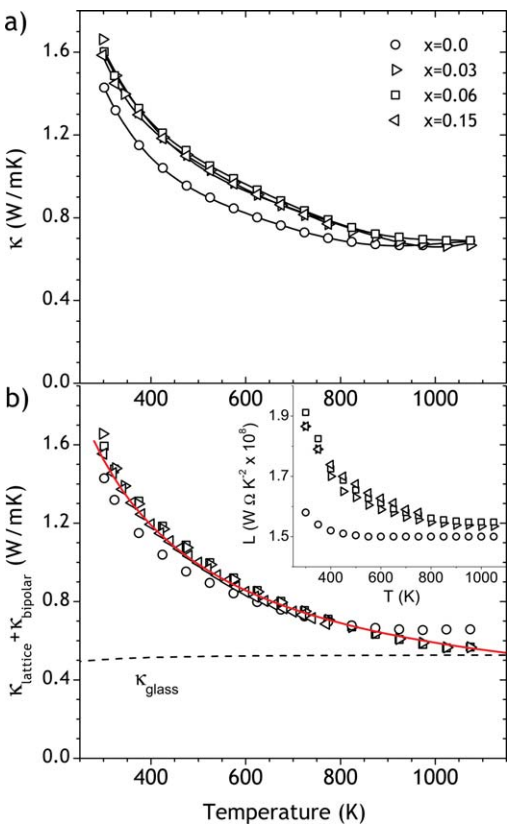

Fig. 15 (a) Total thermal conductivity of $Ca_{3-x}Na_xAlSb_3$ (x = 0, 0.03, 0.06, 0.15). (b) κ_L exhibits 1/T temperature dependence (dashed red curve). At high temperatures, κ_L approaches the glassy limit (dashed black curve). The inset illustrates the temperature dependence of the Lorenz numbers.

estimate the electronic contribution to the thermal conductivity. Temperature dependent Lorenz numbers (L) were calculated within a single parabolic band approximation using eqn (4), assuming a mobility limited by acoustic phonon scattering. The reduced chemical potential, η, was calculated from experimental Seebeck coefficients.

$$L = \left(\frac{k_b}{e}\right)^2 \frac{3F_0(\eta)F_2(\eta) - 4F_1(\eta)^2}{F_0(\eta)^2} \quad (4)$$

In both doped and undoped Ca_3AlSb_3, κ_e is small (<0.08 W/mK), due to the relatively high electrical resistivity, and small Lorenz values (inset, Fig. 15b). Subtracting κ_e from κ_{total} leaves the lattice and bipolar contributions (Fig. 15b). There appears to be a significant bipolar contribution at temperatures above 900 K in the undoped material, while κ_L is the dominant contribution in the doped samples. The temperature dependence of κ_L is well described by the $1/T$ relationship expected for Umklapp scattering (solid red curve). Doping with sodium does not result in a significant change in lattice thermal conductivity, as might be expected for low dopant concentrations and small mass contrast.

Room temperature ultrasonic measurements of undoped Ca_3AlSb_3 yield longitudinal and transverse speeds of sound of 4170 m/s and 2440 m/s respectively. From these, a mean speed of sound of 2710 m/s and an effective Debye temperature of 261 K are calculated using eqn (5) and eqn (6).

$$v_m^3 = \frac{3}{v_l^{-3} + 2v_t^{-3}} \quad (5)$$

$$\theta_D = \frac{v_m \hbar}{k_b}\left(\frac{6\pi^2}{V}\right)^{1/3} \quad (6)$$

An estimate of the lower bound for the lattice thermal conductivity can be made using eqn (7), where the sum is over three vibrational modes (one longitudinal and two transverse) and where $\theta_i = v_i(\hbar/k_b)(6\pi^2/V)^{1/3}$. This model assumes a minimum scattering length as a function of phonon frequency and is often described as the glassy limit of the lattice thermal conductivity.[32]

$$\kappa_{min} = \left(\frac{\pi}{6}\right)^{1/3} \frac{k_b}{V^{2/3}} \sum_i v_i \left(\frac{T}{\theta_i}\right)^2 \int_0^{\theta_i/T} \frac{x^3 e^x}{(e^x - 1)^2} dx \quad (7)$$

At high temperature, κ_L approaches the predicted glassy limit. This low lattice thermal conductivity is most likely a result of the complex crystal structure and large unit cell size of Ca_3AlSb_3. With 28 atoms per unit cell, the phonon dispersion of Ca_3AlSb_3 has a large number of relatively flat optical modes, and therefore, the vast majority of the heat capacity is contained in near-zero group velocity modes which contribute minimally to the lattice thermal conductivity.[3,4] In addition to structural complexity, defect scattering may also have a significant influence on κ_L in this compound.

Figure of merit

The figure of merit of the $x = 0$–0.06 compositions, calculated from the high temperature results presented above, are shown in Fig. 16. The $x = 0.15$ data is not included here, due to the significant presence of the sodium-rich impurity phase. A maximum zT value of 0.8 is obtained at 1050 K for the samples with $x = 0.03$ and $x = 0.06$. In Fig. 17, the experimental zT *versus* carrier concentration is compared to a single parabolic band model (dashed line). We have again focused on transport at 700 K to avoid error associated with activated carriers at higher temperatures and to clearly be in a regime where transport is limited by phonon scattering. The measured Seebeck coefficient and carrier concentration of the $x = 0.06$ sample were used as inputs in eqn (1) and eqn (2) to calculate an effective mass of 0.8 m_e, as described above. Eqn (4) determines the carrier concentration dependence of the Lorenz number, while a constant lattice thermal conductivity (0.78 W/mK) is used. Eqn (8) is used to determine the carrier concentration dependence of the mobility where $\mu_o = 15$ cm^2/V s is calculated from the mobility and reduced chemical potential (η) of the $x = 0.06$ sample at 700 K.

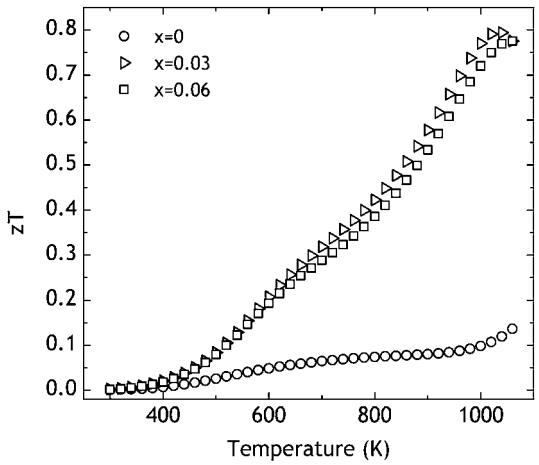

Fig. 16 High temperature figure of merit of $Ca_{3-x}Na_xAlSb_3$ yields a maximum value of 0.8 at 1050 K.

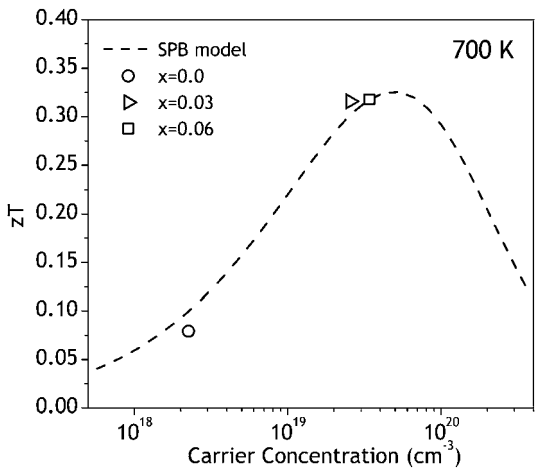

Fig. 17 Experimental zT *versus* carrier concentration for $Ca_{3-x}Na_xAlSb_3$. The dashed line was generated using a single parabolic band model, with an effective mass of 0.8 m_e, an intrinsic mobility of 15 cm^2/Vs and lattice thermal conductivity of 0.78 W/mK.

$$\mu_H = \mu_o \frac{\pi^{1/2} F_\lambda(\eta)}{2\Gamma(1+\lambda) F_{1/2}(\eta)} \quad (8)$$

The maximum carrier concentration obtained experimentally, 4×10^{19} holes/cm^3, is close to the optimum carrier concentration of 5×10^{19} holes/cm^3 predicted by the model at 700 K. However, the maximum zT of this material occurs at higher temperatures, at which point lightly doped material is susceptible to reduction in thermoelectric voltage due to minority carrier activation. A single parabolic band model does not take carrier activation into account, and therefore, while accurate at 700 K, likely underestimates the optimum carrier concentration for a maximum zT at higher temperatures. This, in addition to the likelihood of a heavy band located near −0.13 eV, suggest that higher carrier concentrations will result in higher zT values than reported here.

Conclusion

The exploration of complex Zintl compounds ($Yb_{14}MnSb_{11}$, $CaZn_2Sb_2$, $Ba_8Ga_{16}Ge_{30}$, $CsBi_4Te_6$, $Ca_5Al_2Sb_6$)[10–13,26,30,33] continues to reveal good thermoelectric materials, with properties that can be readily rationalized through simple chemical principles. Here, we have described a new thermoelectric material, Ca_3AlSb_3, a *p*-type semiconductor composed of Earth-abundant, non-toxic elements. Electronic structure calculations suggest that the valence band edge is effectively two nested parabolic bands, which are dominated by Sb *p* states. Carrier concentration control has been achieved by substituting Ca^{+2} with Na^{+1}. High temperature transport properties can be modeled with parabolic bands and acoustic phonon scattering of charge carriers to guide further optimization of the material. The lattice thermal conductivity is found to approach the glassy minimum at high temperature (0.6 W/mK at 1050 K), behavior attributed to a complex unit cell. The combination of low lattice thermal conductivity and a sufficiently large band gap to maintain degenerate behavior at high temperature leads to a zT of 0.8 at 1050 K, with higher zT likely at higher carrier concentrations.

Acknowledgements

We gratefully acknowledge the Jet Propulsion Laboratory, Beckman Foundation, and National Science Foundation for support. We also thank Teruyuki Ikeda for obtaining WDS data and L. D. Zoltan for performing high temperature Seebeck measurements. Espen Flage-Larsen would like to acknowledge support from the Norwegian Research Council and the Norwegian Metacenter for computational Science.

References

1 G. J. Snyder and E. S. Toberer, *Nature Mater.*, 2008, **7**, 105.
2 E. S. Toberer, A. F. May and G. J. Snyder, *Chem. Mater.*, 2009, **22**, 624–634.
3 M. Roufosse and P. G. Klemens, *Phys. Rev. B*, 1973, **7**, 5379–5386.
4 G. A. Slack, *Solid State Physics*, Vol. 34, Academic Press, New York, 1979.
5 L. E. Bell, *Science*, 2008, **321**, 1457.
6 S. M. Kauzlarich, *Chemistry, Structure, and Bonding of Zintl Phases and Ions*, Wiley-VCH, 1996.
7 S. M. Kauzlarich, S. R. Brown and G. J. Snyder, *Dalton Trans.*, 2007, **21**, 2099.
8 G. A. Papoian and R. Hoffmann, *Angewandte Chemie*, 2000, **39**, 2408–2448.
9 M. Mills, R. Lam, M. J. Ferguson, L. Deakin and A. Mar, *Coordination Chem. Rev.*, 2002, **233–234**, 207–222.
10 E. S. Toberer, C. A. Cox, S. R. Brown, T. Ikeda, A. F. May, S. M. Kauzlarich and G. J. Snyder, *Adv. Funct. Mater.*, 2008, **18**, 2795.
11 S. R. Brown, S. M. Kauzlarich, F. Gascoin and G. J. Snyder, *Chem. Mater.*, 2006, **18**, 1873.
12 E. S. Toberer, S. R. Brown, T. Ikeda, S. M. Kauzlarich and G. J. Snyder, *Appl. Phys. Let.*, 2008, **93**(6), 062110.
13 E. S. Toberer, A. Zevalkink and G. J. Snyder, *Adv. Funct. Mater.*, DOI: 10.1002/adfm.201000970.
14 G. Cordier, H. Schaefer and M. Stelter, *Z. Naturforsch*, 1984, **39b**, 727–732.
15 G. Cordier, M. Stelter and H. Schaefer, *J. of Less Common Metals*, 1984, **98**, 285–290.
16 G. Cordier, M. Stelter and H. Schaefer, *Z. Naturforschung*, 1982, **37**, 975–980.
17 H. Schaefer, *Ann. Rev. Mater. Sci*, 1985, **15**, 1–41.
18 G. Cordier, E. Czech, M. Jakowski and H. Schaefer, *Rev. Chemie Minerale*, 1981, **18**, 9–18.
19 C. Wood, D. Zoltan and G. Stapfer, *Rev. Sci. Instruments*, 1985, **56**, 719.
20 G. Kresse and J. Hafner, *Phys. Rev. B*, 1993, **47**, 558–561.
21 G. Kresse and J. Furthmuller, *Comput. Mater. Sci.*, 1996, **6**, 15–50.
22 J. P. Perdew, K. Burke and M. Ernzerhof, *Phys. Rev. Lett.*, 1996, **77**, 3865–3868.
23 G. Kresse and D. Joubert, *Phys. Rev. B*, 1999, **59**, 1758–1775.
24 E. Flage-Larsen, O. M. Løvvik, O. Prytz and J. Taftø, *Comp. Mater. Sci.*, 2010, **47**, 752–757.
25 U. I. Ravich, B. A. Efimova, I. A. Smirnov, *Semiconducting lead chalcogenides*, Plenum Press, 1970.
26 A. F. May, E. S. Toberer, A. Saramat and G. J. Snyder, *Phys. Rev. B*, 2009, **80**, 125205.
27 V. I. Fistul, *Heavily Doped Semiconductors*, Plenum Press, 1969.
28 H. J. Goldsmid and J. W. Sharp, *J. Electron. Mater.*, 1999, **28**, 869.
29 A. F. May, D. J. Singh and G. J. Snyder, *Phys. Rev. B*, 2009, **79**, 153101.
30 E. S. Toberer, A. F. May, B. C. Melot, E. Flage-Larsen and G. J. Snyder, *Dalton Trans.*, 2009, **39**, 1046–10054.
31 D. Sánchez-Portal, R. M. Martin, S. M. Kauzlarich and W. E. Pickett, *Phys. Rev. B*, 2002, **65**, 144414.
32 D. G. Cahill and R. O. Pohl, *Ann. Rev. Phys. Chem.*, 1988, **39**, 93–121.
33 D.-Y. Chung, T. Hogan, P. Brazis, M. Rocci-Lane, C. Kannewurf, M. Bastea, C. Uher and M. Kanatzidis, *Science*, 2000, **287**, 1024–1027.

